Sensitivities of Large Eddy Simulations of Aerosol Plume Transport and Cloud Response

Chandru Dhandapani[1], Colleen M. Kaul[1], Kyle G. Pressel[1], Peter N. Blossey[2], Robert Wood[2], Gourihar Kulkarni[1]

[1]Pacific Northwest National Laboratory, Richland, WA, USA
[2]Department of Atmospheric Sciences, University of Washington, Seattle, USA

Key Points:

- Simulations of plume transport are sensitive to grid spacing, but moderately fine grid spacings may suffice to capture key features.
- Connections between turbulence, scalar mixing, and cloud condensation produce spurious brightening within passive, inert plumes.
- Perturbed area increases weakly with aerosol injection rate, over distances up to several kilometers downstream of the injection point.

Corresponding author: Colleen M. Kaul, `colleen.kaul@pnnl.gov`

Corresponding author: Chandru Dhandapani, `chandru.dhandapani@pnnl.gov`

Abstract

Cloud responses to surface-based sources of aerosol perturbation depend in part on the characteristics of the aerosol transport to cloud base and the resulting spatial and temporal distribution of aerosol. However, interactions among aerosol, cloud, and turbulence processes complicate the prediction of this aerosol transport and can obscure diagnosis of the aerosols' effects on cloud and turbulence properties. Here, scenarios of plume injection below a marine stratocumulus cloud are modeled using large eddy simulations coupled to a prognostic bulk aerosol and cloud microphysics scheme. Both passive plumes, consisting of an inert tracer, and active plumes are investigated, where the latter are representative of saltwater droplet plumes such as have been proposed for marine cloud brightening. Passive plume scenarios show a spurious in-plume cloud brightening due solely to the connections between updrafts, cloud condensation, and scalar transport. Numerical sensitivities are first assessed to establish a suitable model configuration. Then sensitivity to particle injection rate is investigated. Trade-offs are identified between the number of injected particles and the suppressive effect of droplet evaporation on plume loft and spread. Furthermore, as the in-plume brightening effect does not depend significantly on injection rate given a suitable definition of perturbed versus unperturbed regions of the flow, plume area is a key controlling factor on the overall cloud brightening effect of an aerosol perturbation.

Plain Language Summary

Increasing the ability of marine clouds to reflect sunlight by leveraging interactions between clouds and aerosols has been proposed as a means of countering climate change known as marine cloud brightening. However, such proposals rely on the ability to apply suitable aerosol perturbations to the clouds using the atmosphere's own turbulent mixing processes. Here, high-resolution numerical modeling methods are tested and used to investigate the details of aerosol delivery to a marine cloud from a near-surface-based plume.

1 Introduction

Interactions among aerosol, clouds, turbulence, and radiation are complex, involving a variety of processes operating over a wide span of time and length scales. Unraveling these interactions has proven highly challenging, as models are limited in the range of scales they can capture and observation-based investigations suffer from issues such as co-variability of meteorological states and aerosol loads and regime dependence of cloud responses (Michibata et al., 2016; Gryspeerdt et al., 2019; Bender et al., 2019; Possner et al., 2020; Fons et al., 2023). Therefore, considerable interest has centered on aerosol perturbation experiments that, at least to some degree, break the links between meteorological patterns and background aerosol conditions. Such experiments can opportunistically use natural (e.g., volcanoes and wildfires) or anthropogenic (e.g., shipping, urban pollution, and agricultural emissions) aerosol sources (Toll et al., 2019; Christensen et al., 2022; Maudlin et al., 2015) or rely on intentional emissions of aerosol for the specific purpose of studying aerosol cloud interactions, such as performed for the Eastern Pacific Emitted Aerosol Cloud Experiment (EPEACE) field campaign (Russell et al., 2013). Under the latter approach, the potential exists to better characterize the aerosol source. However, the turbulent mixing processes responsible for transporting emitted aerosol to the cloud are not completely understood nor constrained, and thus uncertainty remains in diagnosing aerosol effects on clouds.

It has been long recognized that positive perturbations in aerosol number can increase the number concentration of cloud droplets and lead to increased cloud albedo (Twomey, 1974). Furthermore, the reduction in droplet sizes can suppress precipitation formation and increase longevity of clouds (Albrecht, 1989), although there is also po-

tential for cloud thinning due to increasing entrainment of dry air (Ackerman et al., 2004). Modeling studies have demonstrated that, under certain conditions, prescribed enhancements in aerosol concentrations can delay the subtropical stratocumulus-to-cumulus transition (Erfani et al., 2022), whereas the transition can trigger rapidly when aerosol are removed by drizzle (Yamaguchi et al., 2017). A solar radiation management strategy known as marine cloud brightening (MCB) proposes to harness those cloud responses to aerosol that result in brighter, more extensive, and longer-lived clouds, thereby increasing the cooling effect associated with boundary layer marine clouds. The basic premise involves emission of plumes of saltwater droplets from near the ocean surface that evaporate within the boundary to leave sea-salt aerosol that can be ingested by clouds. Although the MCB concept originated a few decades ago (Latham, 1990), and has been refined since then (Latham, 2002; Latham et al., 2012; Wood, 2021), several key physical science questions remain open. Diamond et al. (2022) identify one of these questions as whether plumes with suitable numbers and sizes of sea-salt aerosol can overcome negative buoyancy associated with saltwater droplet evaporation to be effectively lofted from their near-surface source to the cloud base. For example, modeling work by Jenkins and Forster (2013) compared plumes emitted as droplets versus dry aerosol only. Their simulations showed a suppression of plume rise due to droplet evaporation leading to a reduced albedo change in perturbed clouds, although the degree of difference varied timing of injection within the diurnal cycle and associated changes in boundary layer turbulence structure. Another possible issue with concentrated plume emissions was modeled by Stuart et al. (2013), who found that in-plume coagulation could reduce particle numbers by ten to ninety percent, depending on atmospheric conditions and plume emission characteristics. Thus, various physical processes affecting the delivery of aerosol to clouds base contribute to uncertainties in the feasibility of MCB, even when we set aside questions of those clouds' potential for brightening.

Large eddy simulations (LES) can explicitly simulate many of the scales of turbulent motion responsible for the transport of aerosol plumes to cloud base and relevant for modulating aerosol-cloud interactions. LES studies of aerosol plume lofting and spread, and subsequent cloud response, have identified important regime dependencies of the response: precipitating versus non-precipitating, low versus high free tropospheric moisture, clean versus polluted background aerosol conditions (Jenkins et al., 2013; Wang et al., 2011; Chun et al., 2023). Notably, Wang et al. (2011) also found rapid vertical transport of a plume (consisting of dry aerosol) via updrafts, combined with significantly slower horizontal spreading, causes strong spatial variability in aerosol concentrations. They highlighted the significance of the interactions between spatially heterogeneous aerosol concentrations and existing cloud field variability, consistent with Wang and Feingold (2009).

These studies indicate the importance of accurately capturing the background cloud microphysical and macrophysical state as well as characterizing the temporal and spatial variability of aerosol plume spread (both vertical and horizontal). However, they have neglected droplet evaporation effects on plume spread and/or used coarse horizontal resolutions (50 m to 300 m) relative to the expected size of salt water droplet spraying systems ($\sim$ 1 m). More effort is needed to assess the sensitivities of LES model predictions in relation to modeling techniques, numerical methods, and physical assumptions. Here we undertake such a sensitivity study, focusing on characteristics of plume lofting within several kilometers downstream of an injection source. After describing our general modeling approach and study configuration, we examine the effects of different lateral boundary treatments, horizontal grid resolution, and scalar and momentum advection discretizations. Using a down-selected computational setup, we then investigate the dependence of the results on saltwater droplet injection rate.

2 Modeling Approach

Our study focuses on a well-known marine stratocumulus cloud configuration, the DYCOMS RF02 idealized LES case study originated by Ackerman et al. (2009) and subsequently used in a wide range of investigations probing various aspects of stratocumulus dynamics, cloud macro- and microphysics, and numerical sensitivities (e.g., Davini et al., 2017; Feingold et al., 2015; Morrison et al., 2018; Yamaguchi & Feingold, 2012). We note that the protocol for this case study applies fixed surface heat fluxes and a simplified radiative transfer parameterization that eliminate some possible feedbacks between plume lofting, turbulent transport, and cloud modification, but these simplifications are expected to have limited impacts over the time and spatial scales examined here. Additionally, we rotate the direction of the mean wind to align with the longer axis of a rectangular computational domain (horizontal domain extent of 15 km x 7.5 km; vertical extent of 1.5 km) so that the plume evolution can be tracked over a longer downstream distance.

Simulations are performed using PINACLES (Predicting INteractions of Aerosol and Clouds in Large Eddy Simulation; Pressel & Sakaguchi, 2021). PINACLES is a novel, massively parallel code developed for simulations of three-dimensional atmospheric turbulence, with emphasis on capabilities for modeling boundary layer turbulence and clouds. PINACLES evolves the anelastic equations of motion using efficient, Fourier-transform-based methods to solve the pressure Poisson equation for domains with either periodic or open lateral boundaries, including concurrent nesting of domains. It features a range of advanced options for discretization of scalar and momentum advective terms that are exercised as part of this work.

Plume injection is represented by a set of stationary (i.e., at a fixed location) volumetric source terms applied within the single model grid cell at the lowest model level, near the centerline of the narrow (y) axis of the domain and 1 km from the x-direction inflow boundary. The injection scenarios fall into two main categories. In the first, the injected scalar is an inert tracer that does not modify the flow field. This type of scenario, referred to as a "passive" plume, can be simulated using periodic lateral boundary conditions for the thermodynamic and velocity variables and simple "zeroing" of the plume tracer variable on the boundary. For a passive plume, plume tracer is nominally a number concentration of particles, but these particles do not interact with the background aerosol and cloud fields predicted by the model. Passive plumes are differentiated from "active" plumes, which can modify the flow field. Active plume injection takes the form of source functions for aerosol number and mass and (optionally) liquid water.

These source functions are defined consistently with the treatment of aerosol and cloud microphysics used in this study. This treatment links a two-moment scheme for cloud microphysics (Morrison et al., 2005) to a prognostic treatment of Aitken and accumulation mode aerosol (Wyant et al., 2022) that builds on the work of Berner et al. (2013). Processes of scavenging, coagulation, and activation cause transfer of Aitken mode particles to the accumuluation mode, while the accumulation mode is depleted by autoconversion, accretion, scavenging, and rainout. Both modes are replenished by surface fluxes that are parameterized following Clarke et al. (2006).

Table 1 summarizes the set of one dozen simulations analyzed here. Simulations are differentiated based on the plume type (passive or active, as discussed above), domain type (a single periodic domain or a non-periodic nest within a periodic parent domain), horizontal grid spacing (varying from 40 m to 5 m, with vertical grid spacing fixed at 5 m), advection numerical options (scheme and flux limiter), and the injection rate of particles (ranging from 10^{13} s^{-1} to 10^{17} s^{-1}). Each simulation is identified with a number 1 through 12 for easy reference.

Table 1. Simulation parameters. All simulations use $\Delta z = 5$ m. Advection (Adv.) scheme and flux limiter options are defined in Section 3.2.

Simulation	Plume	Domain	$\Delta x = \Delta y$	Adv. scheme	Flux limiter	Inj. rate
1	Passive	Periodic	40 m	WENO7-Z	EMONO	10^{16} s^{-1}
2	Passive	Periodic	20 m	WENO7-Z	EMONO	10^{16} s^{-1}
3	Passive	Periodic	5 m	WENO7-Z	EMONO	10^{16} s^{-1}
4	Passive	Periodic	20 m	WENO7-Z	No EMONO	10^{16} s^{-1}
5	Passive	Periodic	20 m	WENO5-Z	EMONO	10^{16} s^{-1}
6	Passive	Periodic	20 m	WENO5-Z	No EMONO	10^{16} s^{-1}
7	Passive	Nested	20 m	WENO7-Z	EMONO	10^{16} s^{-1}
8	Active	Nested	20 m	WENO7-Z	EMONO	10^{13} s^{-1}
9	Active	Nested	20 m	WENO7-Z	EMONO	10^{14} s^{-1}
10	Active	Nested	20 m	WENO7-Z	EMONO	10^{15} s^{-1}
11	Active	Nested	20 m	WENO7-Z	EMONO	10^{16} s^{-1}
12	Active	Nested	20 m	WENO7-Z	EMONO	10^{17} s^{-1}

After some preliminary discussion of the metrics we use for comparing simulations, resolution-dependence is assessed by comparing Simulations 1-3 in section 3.1. Next, section 3.2 examines simulations 2, 4-6 for sensitivities to advection scheme numerics. For simplicity, these simulations inject passive plumes within doubly-periodic domains. Prior to analyzing active plume sensitivities, the consistency of our nested and periodic domain results is demonstrated in section 3.3 using data from Simulation 7. Finally, active plume results are presented in section 3.4, focusing on sensitivities to particle injection rate as varied among Simulations 8-12.

3 Results

All simulation data used to produce the figures shown in this section are available online, along with additional supporting materials including plotting notebooks, simulation codes, and input files (Dhandapani, Kaul, & Pressel, 2023; Dhandapani, Kaul, & Blossey, 2023).

All PINACLES simulations presented here evolve similarly following an initial spin up-period of about 90 minutes. Although the simulations do not reach a true steady state, after a few hours changes in the cloud state are gradual. This typical pattern of evolution consists of a slow rise in cloud top that is accompanied by slowly declining liquid water path (LWP), indicative of entrainment of the overlying dry air. A very small amount of drizzle is formed, but almost all evaporates before reaching the surface. Over the downstream distance included in our computational domains (i.e., 14 km), the macroscopic features of the cloud are not significantly changed by the aerosol injection. This does not exclude the possibility that more significant adjustments would occur at a greater distance downstream if the computational domain were expanded. Over the fourth simulated hour, liquid water paths from all simulations using 20 m horizontal resolution vary from 58 to 66 g m^{-2}, and rain water paths range between 0.33 and 0.45 g m^{-2}. Inversion height z_i (as defined by Ackerman et al., 2009) varies almost negligibly from 855 m to 857 m (i.e., differences in z_i are smaller than vertical grid spacing Δz).

Simulations are compared using a variety of quantities to examine both differences in the background cloud and turbulence state and to hone in on the details of plume transport and cloud response. For the former, we compare mean vertical profiles of variables

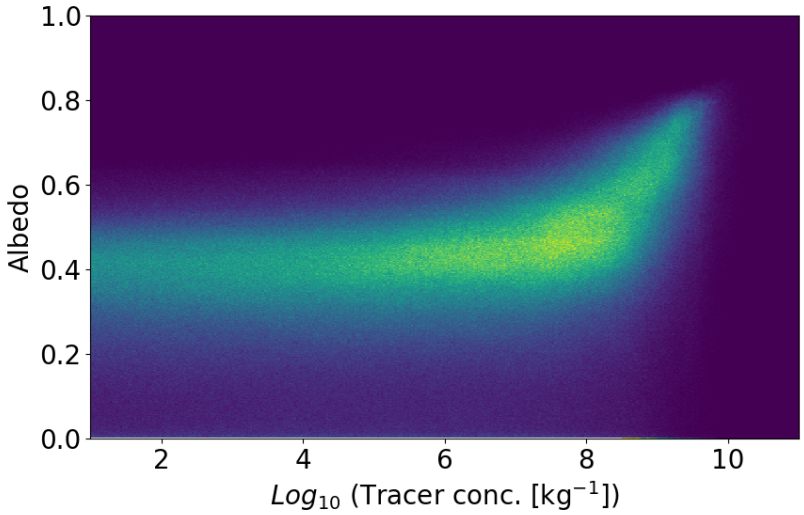

Figure 1. Joint probability distribution function of pseudo-albedo and tracer concentration at 600 m from Simulation 11 between 1.5 and 6 hours.

such as cloud water mixing ratio, droplet number concentration, and vertical velocity variance. For the latter, we compute plume area, plume width, and plume height statistics, and examine differences in cloud brightness in- and out-of plume.

This brightness is estimated by calculating a pseudo-albedo value, α, from the cloud properties as (Szczap et al., 2014),

$$\alpha = \frac{(1-g)\,\tau}{2+(1-g)\,\tau},$$

where $g = 0.86$ is the asymmetry parameter. Optical depth, τ, is calculated as

$$\tau = \frac{3}{2}\int \frac{\rho\, q_c}{r_{\text{eff}}}\, dz,$$

where q_c is the cloud water mixing ratio and r_{eff} is the effective cloud droplet radius predicted by the microphysical scheme consistent with its distributional assumptions. The pseudo-albedo is henceforth referred to as albedo in figure labels for brevity. Note that this pseudo-albedo is a diagnostic quantity only. Radiative heating/cooling rates are parameterized in the simulations following the approach of Ackerman et al. (2009).

Below the cloud base, we assume that scalars associated with the aerosol size distribution act similarly to passive tracers, and thus the plume tracer variable can be used to identify in- and out-of plume regions consistently in both active and passive plume injection scenarios. This assumption is not strictly true: first, due to aerosol processes that may occur below cloud (such as scavenging, which we expect to be small for the weakly precipitating clouds simulated here) and second, due to the nonlinear advection schemes used in these simulations. It nonetheless remains a better option than attempting to identify in-plume regions in the active plume regions from the aerosol fields themselves.

A non-zero lower threshold on plume tracer value is needed to define in- and out-of plume regions that are physically meaningful, but requires some subjective judgment. Figure 1 plots the joint distribution of plume tracer value close to cloud base at 600 m (actually, 602.5 m due to PINACLES' grid staggering, but henceforth referred to as 600

m for conciseness) versus pseudo-albedo of the overlying cloud, obtained from the "baseline" active plume simulation, Simulation 11 of Table 1. Below a value of approximately 10^8 kg^{-1}, albedo and tracer concentration appear virtually uncorrelated, whereas above 10^8 kg^{-1} there is a positively correlated relationship between the two variables. Given that the horizontally-averaged background accumulation mode number concentration at cloud base ranges from 6.5×10^7 kg^{-1} to 8.0×10^7 kg^{-1} (it varies in time due to the surface aerosol flux based on windspeed), this threshold is consistent with a 25-50% perturbation over the background number of accumulation mode particles that would be expected without any plume injection. In the following results, this 10^8 kg^{-1} threshold is used to designate in- and out-of plume regions and to compute plume areas and widths, unless otherwise specified. Additionally, unless otherwise specified, all plume areas are computed at the 600 m vertical level, that approximates the time-averaged cloud-base level.

With these definitions set, we turn to presenting the results of our sensitivity tests. As grid-resolution sensitivity has been frequently noted in LES of stratocumulus clouds (see, for example, the discussion in Matheou & Teixeira, 2019), its effects are examined first, and contrasted with inter-model sensitivities at high resolution.

3.1 Grid resolution and inter-model comparison

Grid resolution sensitivity is assessed by comparing periodic domain, passive plume simulations using 40 m, 20 m, and 5 m horizontal grid spacings, while keeping the vertical grid resolution fixed at 5 m (corresponding to Simulations 1, 2, and 3 of Table 1.) Although it has been shown that grid resolutions finer than 5 m may be required to attain grid convergence of stratocumulus simulations (Matheou & Teixeira, 2019), we note that 5 m isotropic grid spacings are atypically fine, considering the domain size of the simulations. Additionally, the predictions of PINACLES are compared to those of the University of Washington version of the System for Atmospheric Modeling (SAM; Khairoutdinov & Randall, 2003) configured with the same initial and boundary conditions, forcings, and domain size, 5 m horizontal grid spacing, and 5 m vertical grid spacing within the boundary layer. Inter-model differences due to differences in numerical schemes and physical treatments preponderate over intra-model differences due to differing grid resolutions as shown by the results plotted in Figs. 2, 3, and 4. However, some aspects of the PINACLES results are sensitive to the grid spacing.

Mean profiles averaged over 4-6 hours from initialization of the simulations are plotted in Fig. 2. All PINACLES simulations predict nearly identical cloud top height. The cloud water mixing ratio q_c profiles of the 20 m simulation and the fine grid (5 m) simulation are very close to each other, while the coarse grid (40 m) simulation produces lower cloud water content and a higher cloud base. In contrast to the resolution dependence of q_c where the coarse simulation was the outlier, the 40 m and 20 m PINACLES simulations predict similar droplet concentrations, while the 5 m simulation produces a higher droplet number. All three resolutions generate vertical velocity variance profiles with similar shape, but the magnitude of the variance increases in line with the increases in q_c (recall that radiative cooling in these simulations depends on q_c but not on n_c.) SAM predicts higher cloud water content, lower cloud droplet number, and an overall thicker cloud, with cloud base about 200 m lower than simulated by PINACLES at 5 m resolution. SAM's vertical velocity variance profile is shifted with respect to PINACLES' consistent with the change in cloud boundaries.

Figure 3 focuses on resolution-dependence of plume-related features. In the left-hand panel, the time evolution of plume area at 600 m shows a resolution-dependent peak during the spin-up period, but subsequent differences in the average plume area are small among all three resolutions, especially relative to the large temporal variability (the range of which is also similar for all three). Plume area predicted by SAM was computed over

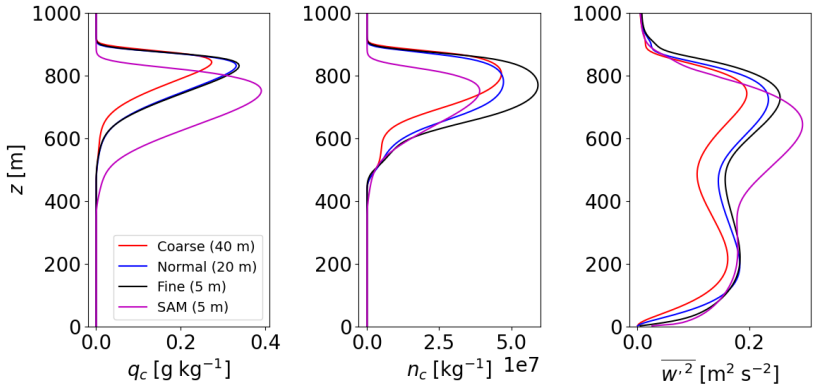

Figure 2. Mean profiles of cloud water mixing ratio (q_c, left), droplet concentration per unit mass (n_c, center), and vertical velocity variance ($\overline{w'^2}$, right) using periodic domains at different grid resolutions. The red, blue, and black curves correspond to horizontal resolutions of 40 m, 20 m, and 5 m, respectively, using PINACLES, and the magenta curves correspond to the SAM simulation (5 m).

the fourth simulated hour, and the average value and one standard deviation range indicated in Figure 3 is comparable to the plume areas obtained from PINACLES. The right hand panel compares the distribution of pseudo-albedo values within in-plume and out-of-plume regions. Notably, the coarsest resolution shows a shift to lower pseudo-albedo values in both regions and especially a heavier left-hand tail of the in-plume pseudo-albedo pdf, indicating more of the plume is co-located with dimmer cloud, or even cloud-free areas. Although the 20 m resolution simulation also produces slightly heavier left-hand tails than the 5 m simulation, the overall agreement is good and the prediction of the right-hand tail is very consistent between the fine and normal resolution simulations.

It should be recalled these results are from passive plume simulations, in which the injected scalar tracer cannot modify the cloud state. Therefore, the higher in-plume pseudo-albedo values shown in Figure 3 indicate that the plume tracer is preferentially lofted to brighter parts of the cloud associated with updrafts.

Besides plume area, the plume width dependence on downstream distance can be defined as an alternative measure of plume spreading. At each downstream transect (taken perpendicular to the long, x axis of the domain), the number of grid points at which the plume tracer value exceeds the in-plume threshold is determined and multiplied by the grid spacing to obtain a width. These widths are additionally averaged in time, with samples available every 60 s. The average plume width values calculated over 3-4 hours from initialization of the simulations are plotted in Fig. 4 for altitudes of 100 m and 600 m. The plume width increases with downstream distance as expected, reaching a nearly linear spread rate at some distance downstream that depends on the vertical level being considered. At 100 m, the plume widths vary with grid resolution and the 5 m PINACLES simulation agrees well with the SAM simulation (5 m). At 600 m, the plume widths are closer to each other for PINACLES simulations at different grid resolutions, and the SAM simulation has higher plume width, possibly because the tracer spreads differently within the cloud than in the subcloud layer (600 m is well within the cloud layer for SAM, but at or below the cloud base for PINACLES.) To examine this possibility further, Figure 5 shows the plume area, averaged in time, as a function of height computed over the full length of the domain and for the final 5 km downstream distance. Plume vertical and horizontal spread are convolved when plume area is computed over the full domain,

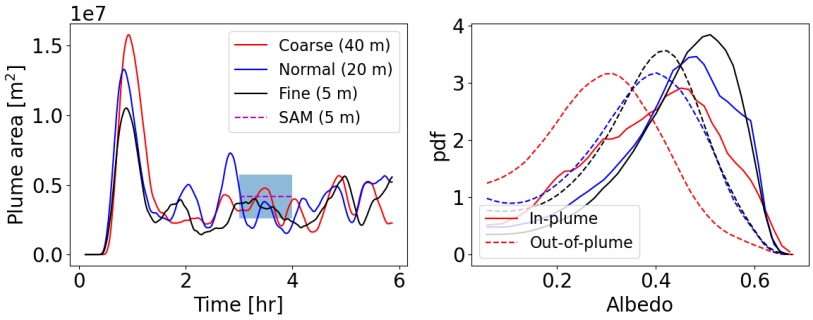

Figure 3. Plume area (left) and pseudo-albedo probability density function (pdf) for in-plume (solid, tracer <10^8 kg^{-1}) and out-of-plume (dashed, tracer <10^8 kg^{-1}) regions, comparing periodic domains at different grid resolutions. The red, blue, and black curves correspond to horizontal resolutions of 40 m, 20 m, and 5 m, respectively, using PINACLES. The dashed magenta line in the left panel corresponds to the mean plume area between hours 3 and 4 from the SAM simulation (at 5 m horizontal resolution) and the gray shaded region is the one standard deviation range from that mean.

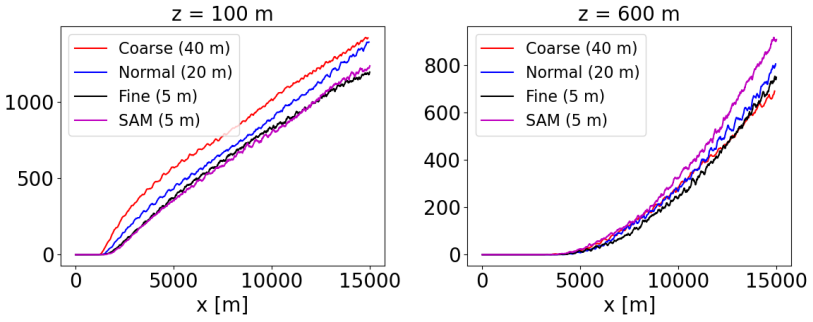

Figure 4. Average plume width at an altitude of 100 m (left) and 600 m (right). The red, blue, and black curves correspond to PINACLES simulations (Simulations 1–3) using horizontal resolutions of 40 m, 20 m, and 5 m, respectively, and the magenta curves correspond to the SAM simulation with a horizontal resolution of 5 m.

but considering only the downstream portion of the domain helps to isolate the horizontal spreading. Below 200 m, plume area is nearly constant with height and decreases with increasing resolution. As expected from Figure 4, 5 m PINACLES and SAM results closely agree. Recall that Figure 2 shows the subcloud vertical velocity variance peak occurs close to 200 m. At 400 m, above the subcloud $\overline{w'^2}$ peak, plume area sharply decreases and continues to diminish to cloud base. However, plume area increases approaching the cloud top, perhaps because additional vertical spread is impeded by the strongly stable cloud-top temperature inversion. Interestingly, and not by design, the differences among all 3 grid resolutions simulated by PINACLES are smallest at the 600 m vertical level that has been the primary focus of our analysis. Therefore, some aspects of the resolution sensitivity might be understated through this focus. Nonetheless, we consider the cloud base emphasis appropriate as it should be most nearly linked to changes in cloud properties when active plumes are introduced.

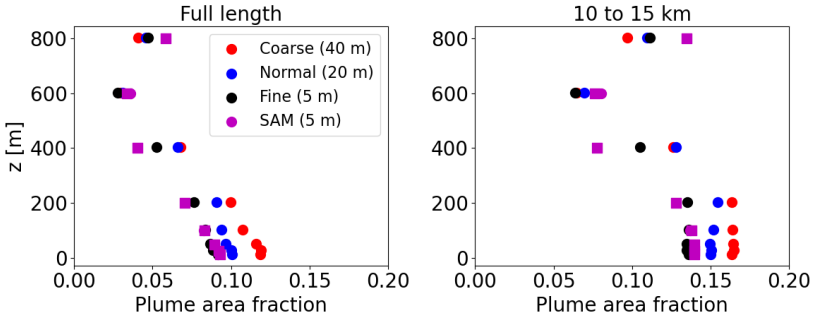

Figure 5. Average plume cross-sectional area fraction plotted against altitude for the full domain (left) and the last 5 km (right) of the domain. The red, blue, and black circles correspond to PINACLES simulations (Simulations 1–3) using horizontal resolutions of 40 m, 20 m, and 5 m, respectively, and the magenta markers correspond to the SAM simulation with a horizontal resolution of 5 m. The circles correspond to averages over every minute between 3 and 4 hours from the start of the simulation and the magenta squares represent the averages of 15-minute samples over the same period (only used for vertical levels without higher frequency data available). The plume area fraction is computed relative to a 14 km by 7.5 km rectangle in the left panel and to a 5 km by 7.5 km rectangle in the right panel.

As the simulation using 20 m horizontal resolution agrees reasonably closely with the 5 m horizontal resolution simulation for most quantities of interest for our comparisons (in particular, the in- and out-of-plume pseudo-albedo contrast is well captured), while drastically reducing the computational cost of simulations, the remaining simulations presented in this work are performed using 20 m horizontal grid spacing.

3.2 Advection schemes

Large eddy simulations of stratocumulus clouds have been shown to be sensitive to the numerical discretization of scalar and momentum advection (Pressel et al., 2017; Matheou & Teixeira, 2019). In particular, different choices of advection scheme (either alone or in concert with subgrid-scale turbulence closures) can strongly change predictions of liquid water path and cloud fraction, especially when the cloud state is sensitive to cloud-top entrainment rate.

As previous work has indicated the superior performance of high-order weighted essentially non-oscillatory (WENO) numerical schemes for simulating stratocumulus clouds (Pressel et al., 2017), we focus on this class of schemes only. In particular, we assess sensitivity to fifth- versus seventh-order forms of a novel implementation of fifth and seventh order WENO-Z schemes (Borges et al., 2008; Castro et al., 2011). Compared to the original WENO schemes (Jiang & Shu, 1996), WENO-Z schemes offer lower dissipation for smooth solutions without increasing computational cost. The WENO-Z schemes implemented in PINACLES feature fully rederived weights and smoothness indicators that are consistent with its finite difference discretization.

Additionally, we evaluate the effects of imposing "essentially monotone" (EMONO) flux limiters on the WENO-Z estimated fluxes. These flux limiters adapt an approach previously applied in conjunction with another scalar flux scheme (Herrmann et al., 2006), such that when a departure from monotonicity is detected, the order of the numerical scheme is locally reduced. Therefore, we compare four simulations (Simulations 2, 4, 5, and 6) from Table 1: fifth- or seventh- order WENO-Z with or without EMONO flux

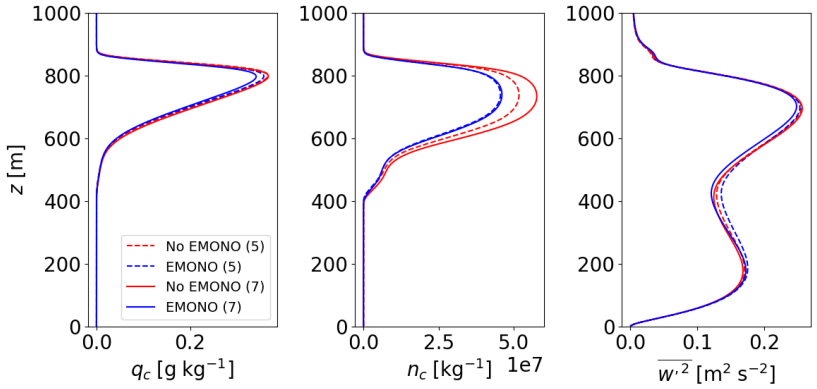

Figure 6. Mean profiles of cloud water mixing ratio (q_c, left), droplet concentration per unit mass (n_c, center), and vertical velocity variance ($\overline{w'^2}$, right) from passive plume simulations (Simulations 2, 4– 6) using WENO5-Z (dashed) and WENO7-Z (solid) schemes, with (blue) and without EMONO flux limiters (red).

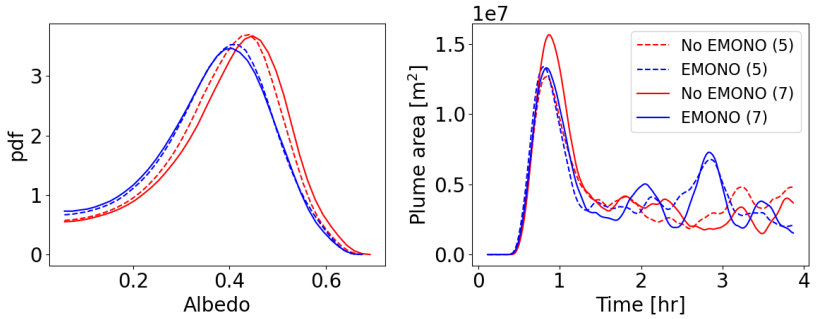

Figure 7. Albedo pdf (left) and time evolution of plume area (right) from passive plume simulations (Simulations 2, 4–6) using WENO5-Z (dashed) and WENO7-Z (solid) schemes, with (blue) and without EMONO flux limiters (red).

limiters. These numerical options are applied to all transported scalars, and the same scheme (without flux limiters) is applied to the velocity fields consistent with the recommendation of Pressel et al. (2017).

The mean profiles from simulations using different advection schemes calculated over 2-4 hours from initialization of the simulations are plotted in Fig. 6. Simulations without EMONO flux limiters agree closely on prediction of q_c and $\overline{w'^2}$, but differ in prediction of n_c with the seventh-order scheme predicting larger droplet number concentration than the fifth-order scheme. In contrast, the fifth-order scheme with EMONO predicts slightly greater q_c and $\overline{w'^2}$ than the seventh-order scheme, but nearly identical n_c. Further examination shows the differences in n_c can be largely attributed to differences in accumulation mode aerosol number concentration, which could be the result of differences in the surface flux of aerosol(which has a strong windspeed dependence) as well as by differences in entrainment of aerosol from the free troposphere. Before moving on, we note that the diagnosed entrainment rate in these simulations over the final two simulated hours is about 0.2 cm s^{-1}, or about one-third the ensemble mean entrain-

ment rate of Ackerman et al. (2009). This reduced entrainment rate is likely related to our choice of numerical schemes.

Entrainment and surface fluxes of aerosol produce domain-averaged aerosol sources to the boundary layer of comparable magnitude [$O(10^{13})$ particles per second], and each varies weakly with numerical scheme. Figure 7 puts these differences in context as producing a small shift towards higher pseudo-albedo values for the simulations that do not use the EMONO flux limiter, which is relatively much smaller than the sensitivity to, say, decreasing the horizontal grid spacing from 40 m to 20 m (Figure 3).

Therefore, we conclude that any of the numerical options presented here can be an acceptable choice, but continue using the seventh-order WENO-Z scheme plus EMONO flux limiter due to the *a priori* preference to be given to higher order, monotone numerics.

3.3 Boundary Conditions

Periodic lateral boundary conditions can be suitable for simulating passive plume emissions as long as the underlying flow field can be treated as periodic. It is straightforward to reset plume tracer values to prevent recirculation of the passive plume. However, active plume emissions are more challenging to simulate satisfactorily with periodic domains as not only the aerosol perturbation but the perturbed cloud and dynamic fields re-enter the domain unless the simulation is truncated after one flow-through time. One strategy is to use a Lagrangian LES approach that follows the evolution of a perturbed airmass in time (Chun et al., 2023). Here, we opt to preserve the Eulerian viewpoint of our passive plume simulations by employing open boundary conditions.

For this purpose, we construct nested domains. The outer, periodic parent is identical to the periodic domain used in the previously described simulations (15 km x 7.5 km x 1.5 km extent, with 20 m horizontal and 5 m vertical grid spacing). An inner child nest receives lateral boundary data from the periodic parent. This inner domain uses the same grid spacing and vertical extent but has slightly reduced horizontal extents due to the placement of the inner lateral boundaries 160 m away from the outer boundaries. Aside from the prescription of the boundary data, the inner child domain evolves independently of its parent. Figure 8 shows the correlation coefficient between instantaneous values of pseudo-albedo and vertical velocity at an altitude of 600 m, calculated over 2-4 hours from initialization of the simulations. Correlations are close to 1 for both variables for distances up to 3 km, but the degree of decorrelation occurring downstream depends on the variable under consideration. Here, pseudo-albedo remains highly correlated between the two domains, but w is more significantly decorrelated between the two domains. It should be noted that the constraint on the horizontal mean vertical velocity ($\langle w \rangle (z) = 0$) that applies for periodic domains under an anelastic approximation can be relaxed on the nest. This has the important implication that the nested domain has greater freedom to respond dynamically to an aerosol perturbation.

When an active plume is simulated, plume injection occurs only on the inner domain so that the periodic parent domain remains undisturbed. To test the nesting procedure, we here inject identical passive plumes on each of the parent and child domains but do not allow plume tracer boundary data to be passed from the parent to the child along with the velocity, thermodynamic, and microphysical prognostic variable boundary data. Although Figure 8 shows that differences develop in point-wise values between the domains, agreement of the plume area statistics (Figure 9) is very close and shows the nesting procedure is performing as expected. Furthermore, these results demonstrate that it is well-founded to compare periodic, passive plume simulations (which are about half as expensive computationally) and nested, active plume simulations on a statistical basis.

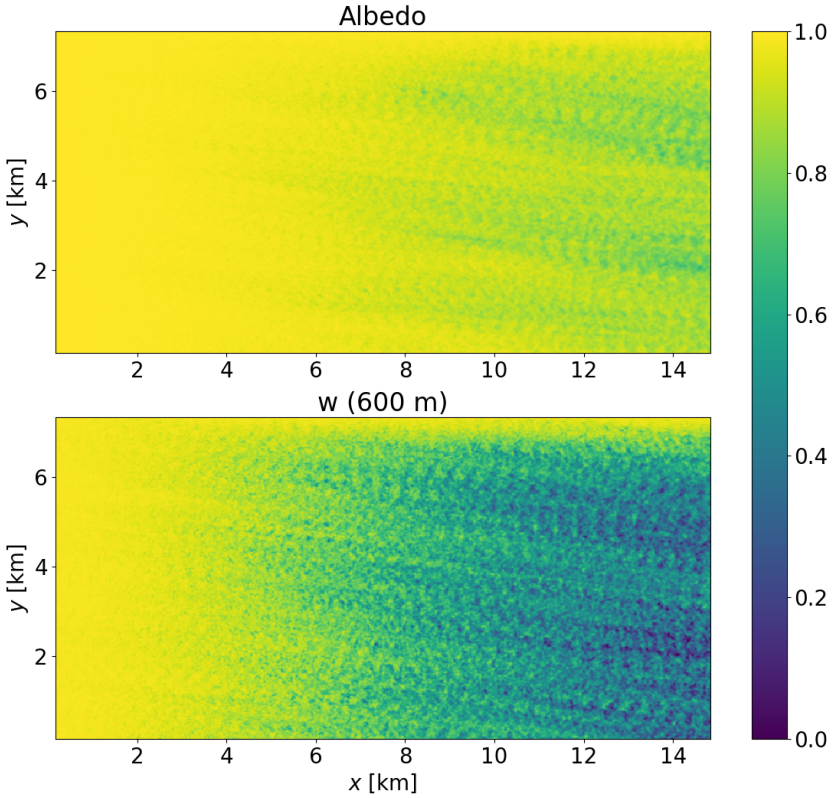

Figure 8. Contour plots of cross-correlation of pseudo-albedo (top) and vertical velocity w at 600 m (bottom) in the periodic parent domain and nested child domain from Simulation 7.

3.4 Injection rates

Nested simulations as described above using active plumes at five different plume injection rates are performed, namely at 10^{13}, 10^{14}, 10^{15}, 10^{16}, and 10^{17} s^{-1}. The maximum injection rate follows the estimate by Salter et al. (2008), although others (Stuart et al., 2013; Wood, 2021) have suggested such high injection rates may not be efficient due to particle coagulation near the source (an effect that is not considered here as the extreme near-field of the particle source is not resolved). Simulations with these varying injection rates are compared to each other and to passive plume simulations to explore the effects of plume injection rates on cloud properties. All simulation presented in this section are restarted from a common checkpoint file after 90 minutes of cloud evolution without any aerosol perturbations applied, and plume injection is commenced at the same time. Thus, the differences in aerosol perturbation do not modify the initial spin-up of the boundary layer and cloud state.

Active plumes

Active plumes are modeled with accumulation mode aerosol of mass mean dry diameter 0.25 μm. This value is based on laboratory measurements from a prototype effervescent nozzle, which produced a sea-salt aerosol population with a mean diameter of 0.12 μm and geometric standard deviation (σ_g) of 2. Notably, this mean diameter of

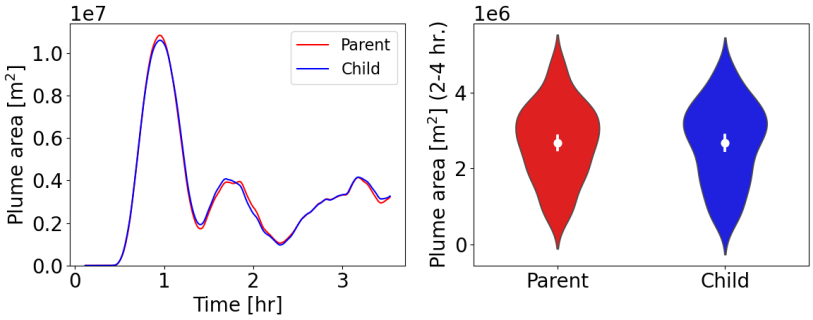

Figure 9. Time evolution of plume area (left) and violin plot of plume area between 2 - 4 hours (right) in the periodic parent domain (red) and nested child domain (blue) nest from Simulation 7.

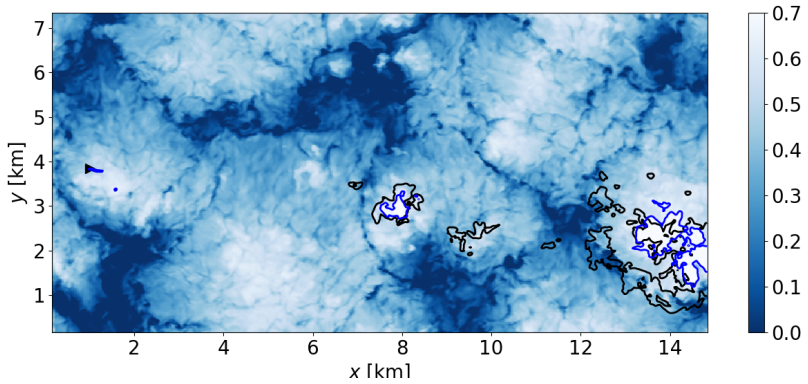

Figure 10. Pseudo-albedo contours calculated 2 hours after initialization of an active plume simulation, Simulation 11, on the nested domain. The black curves correspond to tracer concentration of 10^8 kg^{-1}, at 600 m and the blue curves correspond to a pseudo-albedo value of 0.65. The black triangle on the left shows the position of the plume source near the surface.

injected accumulation mode aerosol is similar to the background accumulation mode, but with a wider distribution. Due to the constraints of the bi-modal, two-moment treatment of aerosol used here, we are not able to fully account for influence of the wider size distribution of the injected aerosol in the cloud response. However, considering an accurate σ_g value is important for estimating the amount of water associated with the plume emission, and hence the potential for plume lofting to be suppressed by evaporative cooling of injected droplets. Each aerosol particle is assumed to be injected within a droplet whose diameter is four times that of the embedded aerosol (Jenkins & Forster, 2013), consistent with an assumed salinity of about 35 g L^{-1} of sea water. The injection rate for the number concentration of accumulation mode aerosol and liquid droplets are set at the same value as that of the passive tracers (10^{13}–10^{17} s^{-1}). For the 10^{16} s^{-1} case, the injection rates for the mass concentrations of accumulation mode aerosol and liquid droplets are calculated from the diameters as 0.1725 kg s^{-1} and 5.1113 kg s^{-1}, respectively (Heintzenberg, 1994), and scaled proportionally for the other injection rates.

The mean profiles for the different injection rates are plotted in Fig. 11. The cloud water mixing ratios are indistinguishable, indicating that no significant liquid water path adjustment occurs over the timescale observable in these simulations (about 30 minutes).

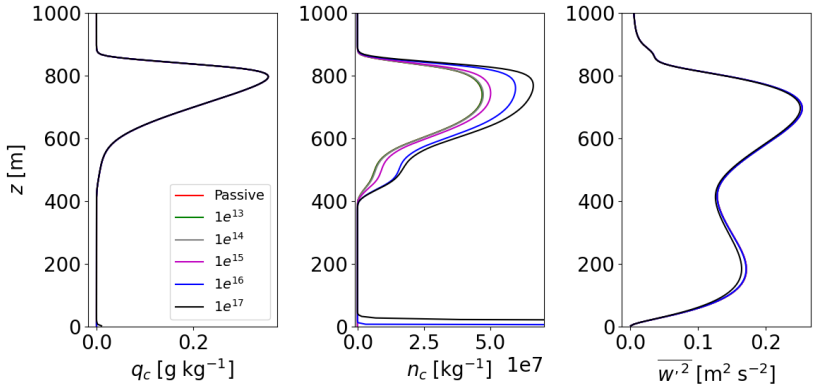

Figure 11. Mean profiles of cloud water mixing ratio (left), droplet concentration (center), and vertical velocity variance (right) using nested domains and active plumes at different injection rates (Simulations 8–12) of 10^{13} (green), 10^{14} (gray), 10^{15} (magenta), 10^{16} (blue), and 10^{17} s^{-1} (black). The red curves correspond to a passive plume (10^{16} s^{-1}) simulation.

To confirm this finding, we computed liquid water path in the parent and child domains of the two highest injection rates over the portions of these domains between $x = 10$ km and $x = 15$ km for a two hour period (2-4 hours). The resulting values are 69.0 g m^{-2} on the parent domains, 68.8 g m^{-2} on the nested domains with 10^{16} s^{-1} injection rate, and 68.4 g m^{-2} on the nested domains with 10^{17} s^{-1} injection rate. While these differences are suggestive of a very slight LWP adjustment, they are too small relative the temporal fluctuations of LWP (6.7 g m^{-2} for all domains) to be confidently interpreted as such. The droplet concentration profiles from the active plume simulations are higher than those of the passive plumes, increasing with injection rates, for values of 10^{15} s^{-1} and higher. When the injection rates are 10^{14} s^{-1} or lower, the domain-averaged droplet concentrations are indistinguishable from that of the passive plumes. The vertical velocity variance profiles are nearly identical, with the 10^{17} s^{-1} simulation showing minor differences that are likely not significant.

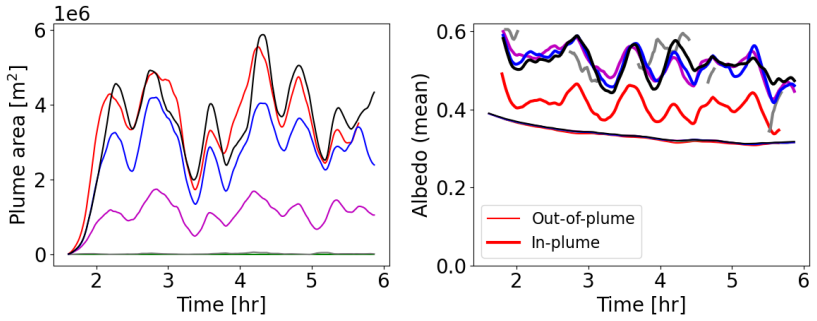

Figure 12. Time evolution of plume area (left) and pseudo-albedo (right) for in-plume (thick lines) and out-of-plume (thin lines) regions using nested domains and active plumes at different injection rates (Simulations 8–12) of 10^{13} (green), 10^{14} (gray), 10^{15} (magenta), 10^{16} (blue), and 10^{17} s^{-1} (black). The red curves correspond to the passive plume (10^{16} s^{-1}) simulation 7.

The time evolutions of plume area near cloud base (namely, at a height of 600 m) and of pseudo-albedo are plotted in Fig. 12. The cloud-base plume area is zero for an injection rate values of 10^{13} s^{-1} and 10^{14} s^{-1}. For injection rates of 10^{15} s^{-1} or higher, the plume area increases with injection rate. The passive plumes (10^{16} s^{-1}) show similar plume area to the 10^{17} s^{-1} case. Active plumes with 10^{16} s^{-1} injection rate have lower plume area than the corresponding passive plumes, due to droplet evaporation. The out-of-plume pseudo-albedo values are exactly the same. The in-plume albedo from all the simulations are higher than that of the out-of-plume albedo. The active plumes show similar in-plume albedo values, regardless of the injection rate values and the passive plume in-plume albedo is not as high as that of active plumes.

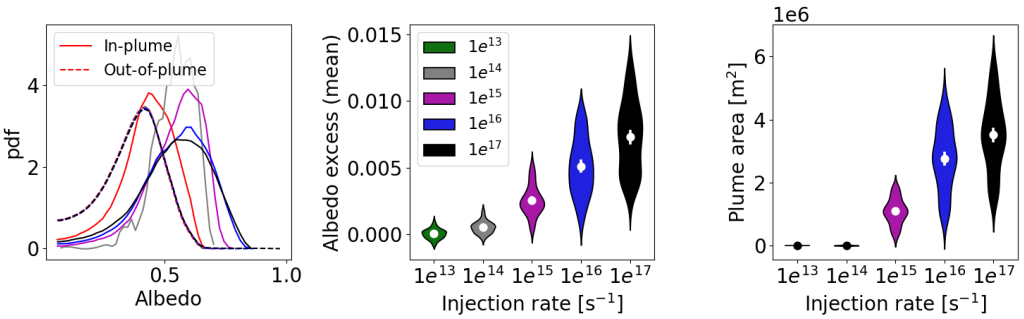

Figure 13. Albedo pdf (left), excess albedo (center) and plume area (right) using nested domains and active plumes at different injection rates (Simulations 8–12), 10^{13} (green), 10^{14} (gray), 10^{15} (magenta), 10^{16} (blue), and 10^{17} s^{-1} (black). The red curves in the left correspond to the passive plume (10^{16} s^{-1}) simulation 7 results.

The pdf of the albedo and violin plots of pseudo-albedo excess (calculated as the difference between the mean pseudo-albedo in the child nest and parent domain) and plume area calculated over 2-4 hours from initialization of the simulations are plotted in Fig. 13. The albedo pdf outside of the plume are indistinguishable from each other, with peak values around 0.4. The pdf of the perturbed cloud albedo values peak around 0.45 for passive plumes and around 0.6 for active plumes with similar distribution profiles. With lower injection rates, the distributions become narrower, missing the tail of the distributions produced by the two highest injection rates, whose agreement suggests the brightening potential of the aerosol perturbation has saturated. Pseudo-albedo excess increases with injection rate. The plume area also increases with injection rate, for 10^{15} s^{-1} and higher rates.

The time evolutions of downstream distance at which plume droplets fully evaporate and mean plume height against downstream distance are plotted in Fig. 14. Note that the microphysics scheme (Morrison et al., 2005) on which the Wyant et al. (2022) aerosol treatment is based uses saturation adjustment to constrain the cloud liquid water mixing ratio and therefore vapor uptake on unactivated aerosols is not included in the moisture budget (however, swollen aerosol size is considered in a diagnostic manner for purposes of computing scavenging rates). For injection rates of 10^{15} s^{-1} and lower, the droplets evaporate immediately. The higher injection rates (10^{16} and 10^{17} s^{-1}) evaporate at downstream distances of 750 m and 3100 m, respectively. The plume heights increase with injection rate and downstream distance until they plateau at the height of the capping inversion. Figure 14 shows two views of this. The middle panel uses unnormalized tracer values, so greater droplet evaporation is combined with overall higher particle numbers as injection rate increases. The middle panel shows that the number

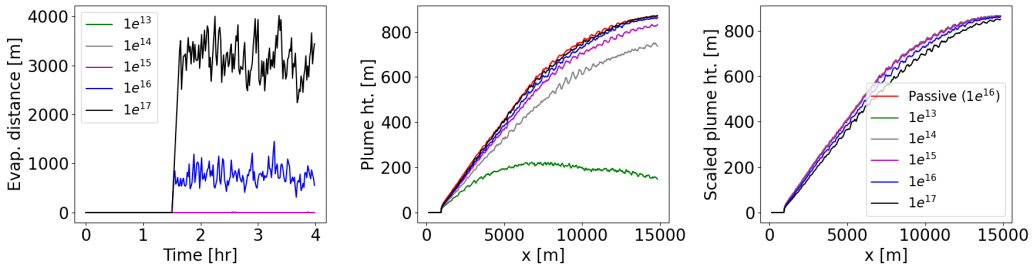

Figure 14. Droplet evaporation distance (left), mean plume height (center) and scaled plume height (right) using nested domains and active plumes at different injection rates (Simulations 8–12): 10^{13} (green), 10^{14} (gray), 10^{15} (magenta), 10^{16} (blue), and 10^{17} s^{-1} (black). The red curves in the right correspond to passive plume (10^{16} s^{-1}) simulation 7 results.

increase effect prevails (i.e., the plume with 10^{17} s^{-1} injection rate rises fastest of the active plumes). However, evaporation does suppress plume rise somewhat, as shown by the difference between the passive and active 10^{16} s^{-1} plume heights). The rightmost panel clarifies these trade-offs. In these results, all inert plume tracers are rescaled to match a 10^{16} s^{-1} injection rate, then thresholding is applied. Here it can be seen that the scaled plume rise is virtually identical in passive plume simulations and active plume simulations with injection rates below 10^{15} s^{-1}. (Scaled) plume rise slows as injection rate increases, but nonetheless the plume is able to reach the inversion by the downstream terminus of the domain.

4 Conclusions

Large eddy simulations can be a powerful means of studying aerosol–cloud interactions. Moreover, they have the potential to accurately represent the interplay between boundary-layer turbulence, aerosol, and clouds, which becomes important when aerosols are distributed inhomogeneously, at small scales, in space or time. An important example of when such a condition may likely occur is one of the proposed approaches for enhancing the albedo of marine clouds by emitting concentrated plumes of sea-salt aerosol just above the sea-surface. The effects of the aerosol perturbation on clouds can only be determined after accounting for the turbulent transport of aerosol from the near-surface. However, previous modeling studies (Wang et al., 2011; Jenkins & Forster, 2013; Chun et al., 2023) have not addressed how their results may be influenced by numerical sensitivities of the LES modeling approach, although the predictions of LES of marine stratocumulus clouds have been found to be sensitive to numerical schemes (Pressel et al., 2017) and grid resolution (Matheou & Teixeira, 2019).

Here we assess these sensitivities for the PINACLES model and design and test an approach to simulate interactive aerosol plumes in idealized setups without undesirable feedback to the nominally upwind flow fields. The model configuration developed through these tests is then used to evaluate how different rates of particle injection affect plume rise and spread and cloud response. We are able to characterize these processes over approximately thirty minutes (estimated based on domain length and boundary-layer wind speed). An important aspect of our selected case is that very limited amounts of precipitation are formed, even in its unperturbed state, and cloud liquid profiles undergo indiscernible adjustment in response to the aerosol perturbation. Thus, changes in brightness are driven by increasing droplet number concentration and decreasing droplet effective radius.

Key findings are:

- Plume area is sensitive to horizontal grid spacings in the range of 5 m to 40 m, especially in the subcloud layer. Resolution sensitivity of plume area decreases within the cloud layer, such that results from 5 m and 20 m grid spacings agree well.
- In-plume enhancement of cloud pseudo-albedo is observed, even for passive (inert tracer) plumes, because of the links between updraft dynamics, plume transport, and condensation. Grid spacings of 20 m or finer are able to characterize the variability of in- and out-of-plume albedo consistently.
- A modeling strategy was developed and demonstrated to allow idealized simulations of active plumes in an Eulerian perspective without recycling of perturbed flow as inflow.
- Subtle differences are observed among simulations using different advection schemes for scalars and momentum, even considering high-order implementations of an advanced family of schemes, that are most apparent in droplet number concentration predictions. The differences in droplet number can be at least partially attributed to differences in aerosol concentration within the boundary layer (even for passive plume cases).
- Using the difference between mean pseudo-albedo on the nested domain and unperturbed periodic parent domain as an indicator of the brightening effect of the injected aerosol, we find injection rates greater than 10^{15} s^{-1} are required and the effect is very limited for injection rates below 10^{15} s^{-1}. However, given that the tracer concentration threshold (10^{8} kg^{-1}) is met, the in-plume albedo enhancement is not significantly different for 10^{16} s^{-1} and 10^{17} s^{-1} injection rates. The overall albedo is somewhat increased at the higher injection rate because the plume area is increased.
- With a fixed threshold for diagnosing the plume extent, a trade-off occurs as particle injection rate raises between making more particles available and increasing the amount of droplet evaporation that suppresses plume rise. In the highest injection rate case, unevaporated droplets can be found over 3 km downstream of the injection point.

These findings indicate several directions for future work. First, more data from measurements and very high-resolution (grid spacings $\ll$ 1 m) simulations are needed to confirm whether the assumptions about the plume injection and immediate near-field properties assumed here are realistic, including microphysical factors such as the particle and droplet size distributions as well as dynamical features such as the momentum source and rate of turbulent entrainment associated with the generation of the plume. Particle loss mechanisms to the surface, parameterized appropriately for use at LES grid resolutions, also need to be considered in more detail, as our simulations may overestimate the potential for initial vertical suppression of plume rise to be compensated farther downstream. At the other extreme, simulations with longer downstream domain extents are needed to understand later stages of plume spread and to track cloud responses over longer time periods to detect feedback with slower timescale processes. Similarly, a wider range of cases that include more strongly precipitating clouds and more realistic radiative flux treatments should also be investigated.

Although open questions remain, the results presented here show clearly the importance of accounting for the interactions of boundary-layer turbulence, droplet evaporation, plume transport, and cloud response and also demonstrate the great utility of carefully performed LES for understanding these interactions. In particular, we find significantly higher in-plume albedo even in passive plume simulations due to the connections among coherent updrafts, plume rise, and cloud formation, and these dynamical and macrophysical linkages must be considered and controlled for when evaluating the impacts of aerosol perturbation strategies on the microphysical process level.

Appendix A Description of PINACLES

Predicting INteractions of Aerosol and Clouds in Large Eddy Simulation (PINACLES) is a modern, parallelized code for three-dimensional simulations of the atmosphere over limited-area domains (Pressel & Sakaguchi, 2021). Although initially developed with a focus on large eddy simulations (and hence its name), it also has capabilities to perform simulations at coarser [O(1 km)] resolutions. The guiding principle of PINACLES' development is optimization for science, which demands consideration of physical fidelity, computational efficiency, and ease of use and extensibility. In this appendix, we focus on describing the general design of PINACLES and those features exercised for the simulations performed for this study, rather than providing a comprehensive description of all currently available model features.

A1 Software Design

PINACLES' dynamical core and input/output features are written in Python, using Numba (Lam et al., 2015) to obtain highly performant code. Because PINACLES is written in Python, it can interface directly with the rich Python toolstack at runtime and easily integrates with a Python-based workflow for configuring, running, and analyzing simulations.

However, as few atmospheric model physics routines are available in Python at present, interfaces to Fortran and C subroutines have been developed. This approach allows a variety of complex parameterizations (e.g., various microphysics schemes, land surface models, radiative transfer models) to be brought online relatively quickly and without incurring the significant upfront cost of a full port to Python. In particular, this approach was used to incorporate the prognostic aerosol scheme of Wyant et al. (2022) used for the simulations of the present study.

A2 Governing Equations

PINACLES solves the anelastic equations of motion, using a thermodynamically consistent variant of the anelastic approximation that retains validity for deep convection scenarios (Pauluis, 2008; Pressel et al., 2015). Prognostic equations are evolved for u, v, and w velocity components, water vapor mixing ratio q_v (defined relative to the reference state density as in Pressel et al., 2015), and a moist static energy s (scaled by the specific heat at constant pressure of air c_p) that is defined as

$$s = T + \left(gz - L_v q_l - L_s q_i\right) c_p^{-1} \tag{A1}$$

where T is the sensible temperature, g is gravitational acceleration, and L_v and L_s are latent heats of vaporization and sublimation, respectively. The summed mixing ratios of liquid- and ice-phase hydrometeors are denoted as q_l and q_i, with the details depending on the choice of microphysics scheme, and additional prognostic equations for hydrometeor mass and number are also solved consistent with the microphysics scheme. In order to ensure numerical conservation of s by the non-linear advection schemes used by PINACLES, the moist static energy as defined in Equation A1 is not directly advected by the model, but rather the advective tendencies of dry, liquid, and ice static energies are computed independently and summed to compute the advective tendency of the moist static energy.

The continuous form equations for momentum, continuity, and scalar transport follow those provided by Pressel et al. (2015). Subgrid-scale turbulent stresses are modeled with a Smagorinsky-Lilly closure (Smagorinsky, 1958, 1963; Lilly, 1962), with adjustment for stable stratification using a buoyancy frequency calculated following Durran and Klemp (1982).

A3 Numerical Discretization

The numerical methods used in PINACLES have been selected to combine low numerical dissipation with good stability.

As mentioned in Section 3.2, PINACLES offers several combinations of options for weighted essentially non-oscillatory schemes for treatment of advection terms. Nominal fifth and seventh order options are available, with traditional (Jiang & Shu, 1996) or "Z" (Borges et al., 2008; Castro et al., 2011) smoothness indicators, and with or without flux limiters (Herrmann et al., 2006) to maintain essentially monotone solutions.

The Poisson equation for pressure is solved non-iteratively using Fourier sine series on periodic domains (see Pressel et al., 2015) and Fourier cosine series on non-periodic domains, the latter approach being similar to techniques used in some other atmospheric models with anelastic dynamical cores (e.g., Lac et al., 2018).

Time integration uses a second-order, two-stage strong stability preserving Runge-Kutta scheme (Shu & Osher, 1988), with adaptive timestep size to hold Courant number below a given limit (here, 0.8).

Appendix B Open Research

The data files and plotting scripts needed to create the figures shown above have been archived at `https://doi.org/10.5281/zenodo.10278509` and `https://doi.org/10.5281/zenodo.10278558`.

These archives also contain the .JSON namelist file for each simulation and a version of the PINACLES code that can be used to perform the simulations listed in Table 1 (using the above mentioned namelist files). A current, general purpose version of PINACLES is available at `https://github.com/pnnl/pinacles`.

Acknowledgments

This research was supported by the Atmospheric System Research (ASR) program as part of the U.S. Department of Energy (DOE) Office of Biological and Environmental Research under Pacific Northwest National Laboratory (PNNL) projects 57131 and 76858. PNNL is operated by DOE by the Battelle Memorial Institute under Contract DE-A06-76RLO 1830. Development of the aerosol-enabled microphysical scheme used in this study was supported by DOE grant DE-SC0020134.

This research used resources of the National Energy Research Scientific Computing Center (NERSC), a U.S. Department of Energy Office of Science User Facility located at Lawrence Berkeley National Laboratory, operated under Contract No. DE-AC02-05CH11231 using NERSC award BER-ERCAP0022771.

We gratefully acknowledge the generous assistance of Matthew Wyant in our use of the aerosol-enabled microphysical scheme described in Wyant et al. (2022). We also thank Renato Pinto Reveggino for his assistance in performing laboratory measurements of spray produced by a prototype nozzle.

Author Contributions: C.D. contributed to PINACLES model development, ran PINACLES simulations, analyzed the results, generated all figures, and wrote portions of the text. C.M.K. contributed to study design, PINACLES model development, interpretation of results, project management, and writing of the text. K.G.P. is the lead designer and developer of PINACLES, and contributed to study design and interpretation of results. P.B. performed SAM modeling and contributed to study design. R. W. contributed to project management and study design. G.K. performed measurements of spray

produced by a prototype effervescent nozzle and contributed to project management. All authors contributed to reviewing and editing the text.

References

Ackerman, A. S., Kirkpatrick, M. P., Stevens, D. E., & Toon, O. B. (2004). The impact of humidity above stratiform clouds on indirect aerosol climate forcing. *Nature*, *432*(7020), 1014–1017. doi: 10.1038/nature03174

Ackerman, A. S., VanZanten, M. C., Stevens, B., Savic-Jovcic, V., Bretherton, C. S., Chlond, A., ... others (2009). Large-eddy simulations of a drizzling, stratocumulus-topped marine boundary layer. *Monthly Weather Review*, *137*(3), 1083–1110. doi: 10.1175/2008MWR2582.1

Albrecht, B. A. (1989). Aerosols, cloud microphysics, and fractional cloudiness. *Science*, *245*(4923), 1227-1230. doi: 10.1126/science.245.4923.1227

Bender, F. A. M., Frey, L., McCoy, D. T., Grosvenor, D. P., & Mohrmann, J. K. (2019). Assessment of aerosol–cloud–radiation correlations in satellite observations, climate models and reanalysis. *Climate Dynamics*, *52*(7), 4371–4392. doi: 10.1007/s00382-018-4384-z

Berner, A. H., Bretherton, C. S., Wood, R., & Muhlbauer, A. (2013). Marine boundary layer cloud regimes and POC formation in a CRM coupled to a bulk aerosol scheme. *Atmospheric Chemistry and Physics*, *13*(24), 12549–12572. doi: 10.5194/acp-13-12549-2013

Borges, R., Carmona, M., Costa, B., & Don, W. S. (2008). An improved weighted essentially non-oscillatory scheme for hyperbolic conservation laws. *Journal of Computational Physics*, *227*(6), 3191-3211. doi: 10.1016/j.jcp.2007.11.038

Castro, M., Costa, B., & Don, W. S. (2011). High order weighted essentially non-oscillatory WENO-Z schemes for hyperbolic conservation laws. *Journal of Computational Physics*, *230*(5), 1766-1792. doi: 10.1016/j.jcp.2010.11.028

Christensen, M. W., Gettelman, A., Cermak, J., Dagan, G., Diamond, M., Douglas, A., ... others (2022). Opportunistic experiments to constrain aerosol effective radiative forcing. *Atmospheric Chemistry and Physics*, *22*(1), 641–674. doi: 10.5194/acp-22-641-2022

Chun, J.-Y., Wood, R., Blossey, P., & Doherty, S. J. (2023). Microphysical, macrophysical, and radiative responses of subtropical marine clouds to aerosol injections. *Atmospheric Chemistry and Physics*, *23*(2), 1345–1368. doi: 10.5194/acp-23-1345-2023

Clarke, A. D., Owens, S. R., & Zhou, J. (2006). An ultrafine sea-salt flux from breaking waves: Implications for cloud condensation nuclei in the remote marine atmosphere. *Journal of Geophysical Research: Atmospheres*, *111*(D6). doi: 10.1029/2005JD006565

Davini, P., D'Andrea, F., Park, S.-B., & Gentine, P. (2017). Coherent structures in large-eddy simulations of a nonprecipitating stratocumulus-topped boundary layer. *Journal of the Atmospheric Sciences*, *74*(12), 4117 - 4137. doi: 10.1175/JAS-D-17-0050.1

Dhandapani, C., Kaul, C. M., & Blossey, P. (2023). *High resolution simulation plume data for sensitivities of large eddy simulations of aerosol plume transport and cloud response.* `https://zenodo.org/records/10278509`. doi: 10.5281/zenodo.10278509

Dhandapani, C., Kaul, C. M., & Pressel, K. G. (2023). *Data and code for sensitivities of large eddy simulations of aerosol plume transport and cloud response.* `https://zenodo.org/records/10278558`. doi: 10.5281/zenodo.10278558

Diamond, M. S., Gettelman, A., Lebsock, M. D., McComiskey, A., Russell, L. M., Wood, R., & Feingold, G. (2022). To assess marine cloud brightening's technical feasibility, we need to know what to study—and when to stop. *Proceedings of the National Academy of Sciences*, *119*(4), e2118379119. doi:

10.1073/pnas.2118379119

Durran, D. R., & Klemp, J. B. (1982). On the effects of moisture on the Brunt-Väisälä frequency. *Journal of Atmospheric Sciences*, *39*(10), 2152–2158. doi: 10.1175/1520-0469(1982)039⟨2152:OTEOMO⟩2.0.CO;2

Erfani, E., Blossey, P., Wood, R., Mohrmann, J., Doherty, S. J., Wyant, M., & O, K.-T. (2022). Simulating aerosol lifecycle impacts on the subtropical stratocumulus-to-cumulus transition using large-eddy simulations. *Journal of Geophysical Research: Atmospheres*, *127*(21), e2022JD037258. doi: 10.1029/2022JD037258

Feingold, G., Koren, I., Yamaguchi, T., & Kazil, J. (2015). On the reversibility of transitions between closed and open cellular convection. *Atmospheric Chemistry and Physics*, *15*(13), 7351–7367. doi: 10.5194/acp-15-7351-2015

Fons, E., Runge, J., Neubauer, D., & Lohmann, U. (2023). Stratocumulus adjustments to aerosol perturbations disentangled with a causal approach. *npj Climate and Atmospheric Science*, *6*(1), 130. doi: 10.1038/s41612-023-00452-w

Gryspeerdt, E., Goren, T., Sourdeval, O., Quaas, J., Mülmenstädt, J., Dipu, S., ... Christensen, M. (2019). Constraining the aerosol influence on cloud liquid water path. *Atmospheric Chemistry and Physics*, *19*(8), 5331–5347. doi: 10.5194/acp-19-5331-2019

Heintzenberg, J. (1994). Properties of the log-normal particle size distribution. *Aerosol Science and Technology*, *21*(1), 46-48. doi: 10.1080/02786829408959695

Herrmann, M., Blanquart, G., & Raman, V. (2006). Flux corrected finite-volume scheme for preserving scalar boundedness in large-eddy simulations. In *43rd AIAA Aerospace Sciences Meeting and Exhibit.* doi: 10.2514/6.2005-1282

Jenkins, A., & Forster, P. (2013). The inclusion of water with the injected aerosol reduces the simulated effectiveness of marine cloud brightening. *Atmospheric Science Letters*, *14*(3), 164–169. doi: 10.1002/asl2.434

Jenkins, A., Forster, P., & Jackson, L. (2013). The effects of timing and rate of marine cloud brightening aerosol injection on albedo changes during the diurnal cycle of marine stratocumulus clouds. *Atmospheric Chemistry and Physics*, *13*(3), 1659–1673. doi: 10.5194/acp-13-1659-2013

Jiang, G.-S., & Shu, C.-W. (1996). Efficient implementation of weighted ENO schemes. *Journal of Computational Physics*, *126*(1), 202–228. doi: 10.1006/jcph.1996.0130

Khairoutdinov, M. F., & Randall, D. A. (2003). Cloud resolving modeling of the arm summer 1997 iop: Model formulation, results, uncertainties, and sensitivities. *Journal of the Atmospheric Sciences*, *60*(4), 607 - 625. doi: 10.1175/1520-0469(2003)060⟨0607:CRMOTA⟩2.0.CO;2

Lac, C., Chaboureau, J.-P., Masson, V., Pinty, J.-P., Tulet, P., Escobar, J., ... Wautelet, P. (2018). Overview of the Meso-NH model version 5.4 and its applications. *Geoscientific Model Development*, *11*(5), 1929–1969. doi: 10.5194/gmd-11-1929-2018

Lam, S. K., Pitrou, A., & Seibert, S. (2015). Numba: A LLVM-based Python JIT compiler. In *Proceedings of the Second Workshop on the LLVM Compiler Infrastructure in HPC.* New York, NY, USA: Association for Computing Machinery. doi: 10.1145/2833157.2833162

Latham, J. (1990). Control of global warming? *Nature*, *347*(6291), 339–340. doi: 10.1038/347339b0

Latham, J. (2002). Amelioration of global warming by controlled enhancement of the albedo and longevity of low-level maritime clouds. *Atmospheric Science Letters*, *3*(2-4), 52-58. doi: 10.1006/asle.2002.0099

Latham, J., Bower, K., Choularton, T., Coe, H., Connolly, P., Cooper, G., ... others (2012). Marine cloud brightening. *Philosophical Transactions of the Royal Society A: Mathematical, Physical and Engineering Sciences*, *370*(1974),

4217–4262. doi: 10.1098/rsta.2012.0086

Lilly, D. K. (1962). On the numerical simulation of buoyant convection. *Tellus*, *14*(2), 148–172. doi: 10.1111/j.2153-3490.1962.tb00128.x

Matheou, G., & Teixeira, J. (2019). Sensitivity to physical and numerical aspects of large-eddy simulation of stratocumulus. *Monthly Weather Review*, *147*(7), 2621 - 2639. doi: 10.1175/MWR-D-18-0294.1

Maudlin, L., Wang, Z., Jonsson, H., & Sorooshian, A. (2015). Impact of wildfires on size-resolved aerosol composition at a coastal California site. *Atmospheric Environment*, *119*, 59-68. doi: 10.1016/j.atmosenv.2015.08.039

Michibata, T., Suzuki, K., Sato, Y., & Takemura, T. (2016). The source of discrepancies in aerosol–cloud–precipitation interactions between GCM and A-Train retrievals. *Atmospheric Chemistry and Physics*, *16*(23), 15413–15424. doi: 10.5194/acp-16-15413-2016

Morrison, H., Curry, J. A., & Khvorostyanov, V. I. (2005). A new double-moment microphysics parameterization for application in cloud and climate models. part i: Description. *Journal of the Atmospheric Sciences*, *62*(6), 1665 - 1677. doi: 10.1175/JAS3446.1

Morrison, H., Witte, M., Bryan, G. H., Harrington, J. Y., & Lebo, Z. J. (2018). Broadening of modeled cloud droplet spectra using bin microphysics in an Eulerian spatial domain. *Journal of the Atmospheric Sciences*, *75*(11), 4005 - 4030. doi: 10.1175/JAS-D-18-0055.1

Pauluis, O. (2008). Thermodynamic consistency of the anelastic approximation for a moist atmosphere. *Journal of the Atmospheric Sciences*, *65*(8), 2719 - 2729. doi: 10.1175/2007JAS2475.1

Possner, A., Eastman, R., Bender, F., & Glassmeier, F. (2020). Deconvolution of boundary layer depth and aerosol constraints on cloud water path in subtropical stratocumulus decks. *Atmospheric Chemistry and Physics*, *20*(6), 3609–3621. doi: 10.5194/acp-20-3609-2020

Pressel, K. G., Kaul, C. M., Schneider, T., Tan, Z., & Mishra, S. (2015). Large-eddy simulation in an anelastic framework with closed water and entropy balances. *Journal of Advances in Modeling Earth Systems*, *7*(3), 1425-1456. doi: 10.1002/2015MS000496

Pressel, K. G., Mishra, S., Schneider, T., Kaul, C. M., & Tan, Z. (2017). Numerics and subgrid-scale modeling in large eddy simulations of stratocumulus clouds. *Journal of Advances in Modeling Earth Systems*, *9*(2), 1342-1365. doi: 10.1002/2016MS000778

Pressel, K. G., & Sakaguchi, K. (2021). *Developing and testing capabilities for simulating cases with heterogeneous land/water surfaces in a novel atmospheric large eddy simulation code* (Tech. Rep.). Pacific Northwest National Laboratory (PNNL), Richland, WA (United States). doi: 10.2172/1869291

Russell, L. M., Sorooshian, A., Seinfeld, J. H., Albrecht, B. A., Nenes, A., Ahlm, L., ... others (2013). Eastern Pacific Emitted Aerosol Cloud Experiment. *Bulletin of the American Meteorological Society*, *94*(5), 709–729. doi: 10.1175/BAMS-D-12-00015.1

Salter, S., Sortino, G., & Latham, J. (2008). Sea-going hardware for the cloud albedo method of reversing global warming. *Philosophical Transactions of the Royal Society A: Mathematical, Physical and Engineering Sciences*, *366*(1882), 3989-4006. doi: 10.1098/rsta.2008.0136

Shu, C.-W., & Osher, S. (1988). Efficient implementation of essentially non-oscillatory shock-capturing schemes. *Journal of Computational Physics*, *77*(2), 439-471. doi: 10.1016/0021-9991(88)90177-5

Smagorinsky, J. (1958). On the numerical integration of the primitive equations of motion for baroclinic flow in a closed region. *Monthly Weather Review*, *86*(12), 457 - 466. doi: 10.1175/1520-0493(1958)086⟨0457:OTNIOT⟩2.0.CO;2

Smagorinsky, J. (1963). General circulation experiments with the primitive equa-

tions: I. The basic experiment. *Monthly Weather Review*, *91*(3), 99 - 164. doi: 10.1175/1520-0493(1963)091⟨0099:GCEWTP⟩2.3.CO;2

Stuart, G. S., Stevens, R. G., Partanen, A.-I., Jenkins, A. K. L., Korhonen, H., Forster, P. M., ... Pierce, J. R. (2013). Reduced efficacy of marine cloud brightening geoengineering due to in-plume aerosol coagulation: parameterization and global implications. *Atmospheric Chemistry and Physics*, *13*(20), 10385–10396. doi: 10.5194/acp-13-10385-2013

Szczap, F., Gour, Y., Fauchez, T., Cornet, C., Faure, T., Jourdan, O., ... Dubuisson, P. (2014). A flexible three-dimensional stratocumulus, cumulus and cirrus cloud generator (3DCLOUD) based on drastically simplified atmospheric equations and the Fourier transform framework. *Geoscientific Model Development*, *7*(4), 1779–1801. doi: 10.5194/gmd-7-1779-2014

Toll, V., Christensen, M., Quaas, J., & Bellouin, N. (2019). Weak average liquid-cloud-water response to anthropogenic aerosols. *Nature*, *572*(7767), 51–55. doi: 10.1038/s41586-019-1423-9

Twomey, S. (1974). Pollution and the planetary albedo. *Atmospheric Environment (1967)*, *8*(12), 1251–1256. doi: 10.1016/0004-6981(74)90004-3

Wang, H., & Feingold, G. (2009). Modeling mesoscale cellular structures and drizzle in marine stratocumulus. Part II: The microphysics and dynamics of the boundary region between open and closed cells. *Journal of the Atmospheric Sciences*, *66*(11), 3257–3275. doi: 10.1175/2009JAS3120.1

Wang, H., Rasch, P. J., & Feingold, G. (2011). Manipulating marine stratocumulus cloud amount and albedo: a process-modelling study of aerosol-cloud-precipitation interactions in response to injection of cloud condensation nuclei. *Atmospheric Chemistry and Physics*, *11*(9), 4237–4249. doi: 10.5194/acp-11-4237-2011

Wood, R. (2021). Assessing the potential efficacy of marine cloud brightening for cooling Earth using a simple heuristic model. *Atmospheric Chemistry and Physics*, *21*(19), 14507–14533. doi: 10.5194/acp-21-14507-2021

Wyant, M. C., Bretherton, C. S., Wood, R., Blossey, P. N., & McCoy, I. L. (2022). High free-tropospheric Aitken-mode aerosol concentrations buffer cloud droplet concentrations in large-eddy simulations of precipitating stratocumulus. *Journal of Advances in Modeling Earth Systems*, *14*(6), e2021MS002930. doi: 10.1029/2021MS002930

Yamaguchi, T., & Feingold, G. (2012). Technical note: Large-eddy simulation of cloudy boundary layer with the Advanced Research WRF model. *Journal of Advances in Modeling Earth Systems*, *4*(3). doi: 10.1029/2012MS000164

Yamaguchi, T., Feingold, G., & Kazil, J. (2017). Stratocumulus to cumulus transition by drizzle. *Journal of Advances in Modeling Earth Systems*, *9*(6), 2333-2349. doi: 10.1002/2017MS001104